Magnetic tunable photonic band-gap structures

by

Nagapratima Kunapareddy

A thesis submitted to the graduate faculty

in partial fulfillment of the requirements for the degree of

MASTER OF SCIENCE

Major: Electrical Engineering

Program of Study Committee:
Shanker Balasubramaniam, Major Professor
Mani Mina
Paul Sacks

Iowa State University

Ames, Iowa

2003

Graduate College
Iowa State University

This is to certify that the master's thesis of

Nagapratima Kunapareddy

has met the thesis requirements of Iowa State University

Signatures have been redacted for privacy

DEDICATION

To Uma, Chen and Anu

TABLE OF CONTENTS

LIST OF FIGURES

ABSTRACT

In this thesis, an integral equation scheme for the analysis of periodic photonic band-gap structures has been discussed. The integral equation is cast in terms of electric flux density and magnetic flux density. A solution is constructed using the method of moments (MoM) by choosing vector basis functions that satisfy the requisite boundary condition. In order to extend the integral equation scheme for the analysis of periodic structures, periodic Green's function is incorporated into this scheme. This scheme is applied to photonic band-gap (PBG) structures and serves to demonstrate that a change in the material constant of the medium can be used to shift the band-gap spectrum of a PBG structure. It has been proposed that band-gap tuning be affected by means of an externally applied field. This renders photonic band-gap structures to useful applications like high-Q filters, optical switches, cavities, lasers, antennas etc.

CHAPTER 1 INTRODUCTION

1.1 Periodic structures

Periodic structures are abundant in nature and their interaction with electromagnetic waves results in the formation of allowed and forbidden energy states. This results in distinct frequency characteristics like stop-bands, pass-bands and band-gaps a feature that renders them well to several applications in optoelectronics and communications. Typical applications include frequency selective structures (FSS), PBG crystals, high Q lasers, wave-guide T-bends, optical interconnects, channel add-drop filters and micro-strip patch antennas, photonic fibers. Introducing a defect in this periodic structure affects the properties of this structure; band-gap properties can be tailored by changing the nature of the defect: size, shape, form, material constant etc. This has led to a new branch of nanostructures called band-gap engineering.

1.2 Photonic band-gap structures

A class of materials which can affect the photon properties is termed as photonic crystals. Pioneering work in this field was conducted by Eli Yablanovitch and Sajeev John. A photonic crystal is a material that possesses a periodic index of refraction A photonic structure is a periodic arrangement of materials with different material constants. Depending on the size, shape and composition of the unit cells, light propagates differently in the photonic crystal. PBGs can be one-dimensional: multilayered films, Bragg stacks, two-dimensional: arrangements of dielectric cylinders [4] or columns or similarly shaped holes in a substrate, or three dimensional: wood-pile structures, diamond lattices) [1]. Photonic band-gap structures can be realized by having a periodic arrangement of air-holes in a dielectric substrate or a lattice of high refractive index material embedded within a medium of a lower refractive index. Typically it is observed

that dielectrics embedded in a lower refractive index medium have smaller band-gaps. Of late $GaAs$ compounds have also been used to construct near-optical photonic crystals [6, 7]

The first photonic crystal was produced by Yablanovitch and his group in 1991 by drilling holes a millimeter in diameter into a block of material of refractive index of 3.6 [10, 11]. This material known as Yablanovite was the first structure to exhibit a 3-D band-gap. A 3-D band-gap, also called a *complete* band-gap occurs when the band-gap range overlaps for all 4π steradian. A crystal with a complete gap serves as an ideal mirror for light along all directions. Early theoretical investigations explored several crystal structures for a 3-D band-gap. Notable among these are the face centered cubic (FCC) crystal [2, 11], the diamond lattices , simple cubic [3] crystals.

Another example of a PBG with a 3-D band-gap was the wood-pile structure, proposed by the Ames Laboratory. Sandia National Laboratories found a technique for the mass-production of these structures in 1999 [12].

1.3 Literature review

As mentioned earlier, the theoretical foundations for the analysis of PBGs was laid by Eli Yablanovitch and Sajeev John. A plane-wave expansion method was used to analyze dielectric PBGs by the Ames Laboratory group [13] in 1990. It must be noted that plane wave methods are expensive in terms of time and memory and inaccurate as they are unable to model discontinuities in the permittivity [14]. An efficient finite difference method for periodic structures was used for computation of propagation constants of guided wave propagating in arbitrary directions [15]. This method, however is not amenable to the E-field formulation. Y. Rahmat-Samii and H. Mosallaei used a more efficient finite difference time domain (FDTD) method with periodic boundary condition/perfectly matched layer (PBC/PML) for the characterization of different types of band-gap structures [16]. Prony's extrapolation scheme was used to accelerate this method. Finite Element methods have also been proposed to model these structures [18]; however they need boundary conditions to be explicitly imposed. The Transfer Matrix Method (TMM) has also gained much popularity in recent years; in this

method the material is subdivided into an number of parallel plates and Maxwell's equations are discretized in the time-domain. The transverse fields, both electric and magnetic, of one unit cell are related to another by approximately estimating the propagation constant in terms of the lattice dimensions of the unit cell [19]. Other computational methods used to analyze PBGs are the time dependent beam propagation method [20], Green's function method using vector Wannier functions [21].

Tunability in PBGs is of enormous importance for several applications like filters, optical switches, cavities, lasers, antennas etc. It is a well-known fact that in non-magnetic materials, periodic variation of refractive index can be used to tune the band-gap spectrum. C.-S. Kee's group stressed the role of wave impedance as opposed to permeability or permittivity in tuning the band-gap [22] and demonstrated this fact for magnetic photonic crystals [8].

In this thesis, an integral equation (IE) based approach is proposed for the analysis of tunable photonic band-gap structures. In IE methods, the Green's functions used in the integral equation based techniques implicitly account for the boundary conditions as opposed to finite-element and finite difference methods. Therein lies the advantage of IE methods. The integral equation is solved using vector basis functions that impose normal continuity of the fields [23]. The integral equation is validated by comparing the far-field patterns of a sphere obtained numerically against analytical results. Validation of the periodic green's function has been done by comparing the transmission spectra from a continuous slab against analytical results.

It is further demonstrated that by changing the effective dielectric and magnetic properties of the medium, a shift in the band-gap can be affected. These properties can changed by the application of an external field. Band-gap tuning is thus achieved by means of an external magnetic field, of particular application in sensor applications.

1.4 Organization

This thesis is organized as follows: Chapter 2 outlines the combined-field volume integral equation for the frequency-domain problem and its conversion to a matrix equation using

the method of moments (MoM). Chapter 3, briefly describes the validity of this method by means of several test cases - first purely dielectric bodies, purely magnetic bodies and later on dielectric and magnetic bodies. The scheme described in Chapter 2 is tested and tunability of the structure is demonstrated in Chapter 4 by means of several test cases. These adequately serve to demonstrate the applicability of this scheme to the modelling and analysis of various band-gap structures. Finally, Chapter 5 summarizes the contribution of this work.

CHAPTER 2 FORMULATION OF THE INTEGRAL EQUATION

In this Chapter, a combined field volume integral equation is derived. The solution to this equation is obtained by discretizing it wherein the flux is represented using a set of basis that have finite support. This naturally leads to a matrix equation that will be solved for both the electric and magnetic flux densities. In what follows, we shall derive the appropriate equations and elucidate the procedure necessary for obtaining a matrix equation.

2.1 Description of the problem

Consider an inhomogeneous body with magnetic permeability $\mu(\mathbf{r})$ and electric permittivity $\epsilon(\mathbf{r})$ occupying a volume V in free space and bounded by a surface S. The body is assumed to be isotropic and is immersed in an ambient electric and magnetic fields given by $\mathbf{E}^i(\mathbf{r})$ and $\mathbf{H}^i(\mathbf{r})$ respectively. The incident field may have arbitrary polarization and direction of propagation. The time dependence is implicit and assumed to be $e^{j\omega t}$.

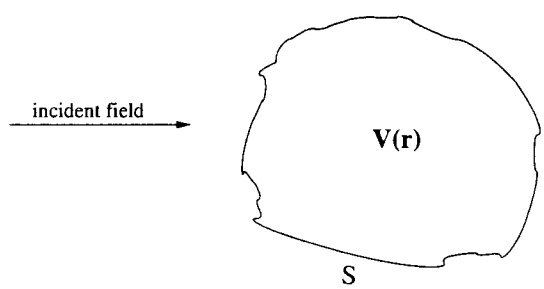

Figure 2.1 Inhomogeneous body immersed in an ambient electric and magnetic fields.

The presence of the body perturbs the field and the total electric and magnetic fields can

be written as :

$$\mathbf{E}^t(\mathbf{r}) = \mathbf{E}^i(\mathbf{r}) + \mathbf{E}^s(\mathbf{r}) \tag{2.1}$$

and

$$\mathbf{H}^t(\mathbf{r}) = \mathbf{H}^i(\mathbf{r}) + \mathbf{H}^s(\mathbf{r}) \tag{2.2}$$

2.2 Formulation of the integral equation

The scattered electric and magnetic fields may be represented in terms of the vector potentials $\mathbf{A}(\mathbf{r})$ and $\mathbf{F}(\mathbf{r})$ and the scalar potentials $\phi^e(\mathbf{r})$ and $\phi^h(\mathbf{r})$ as

$$\mathbf{E}^s(\mathbf{r}) = -j\omega\mathbf{A}(\mathbf{r}) - \nabla\phi^e(\mathbf{r}) - \frac{1}{\epsilon_o}\nabla \times \mathbf{F}(\mathbf{r}) \tag{2.3}$$

$$\mathbf{H}^s(\mathbf{r}) = -j\omega\mathbf{F}(\mathbf{r}) - \nabla\phi^h(\mathbf{r}) + \frac{1}{\mu_o}\nabla \times \mathbf{A}(\mathbf{r}) \tag{2.4}$$

where

$$\mathbf{A}(\mathbf{r}) = \frac{\mu_o}{4\pi}\int_v \mathbf{J}(\mathbf{r}')\frac{e^{-jkR}}{\mathbf{R}}dv' \tag{2.5}$$

$$\mathbf{F}(\mathbf{r}) = \frac{\epsilon_o}{4\pi}\int_v \mathbf{M}(\mathbf{r}')\frac{e^{-jkR}}{\mathbf{R}}dv' \tag{2.6}$$

$$\phi^e(\mathbf{r}) = \frac{1}{4\pi\epsilon_o}\int_v \boldsymbol{\rho}^e(\mathbf{r}')\frac{e^{-jkR}}{\mathbf{R}}dv' \tag{2.7}$$

$$\phi^h(\mathbf{r}) = \frac{1}{4\pi\mu_o}\int_v \boldsymbol{\rho}^h(\mathbf{r}')\frac{e^{-jkR}}{\mathbf{R}}dv' \tag{2.8}$$

$k = \omega\sqrt{\mu_o\epsilon_o}$ is the free space wave number. In the above equations, $R = |\mathbf{r} - \mathbf{r}'|$ denotes the distance between the source and the observer points. The equivalent volume currents $\mathbf{J}(\mathbf{r})$ and $\mathbf{M}(\mathbf{r})$ are represented as

$$\mathbf{J}(\mathbf{r}) = j\omega(\epsilon(\mathbf{r}) - \epsilon_o)\mathbf{E}(\mathbf{r}) \tag{2.9}$$

and

$$\mathbf{M}(\mathbf{r}) = j\omega(\mu(\mathbf{r}) - \mu_o)\mathbf{H}(\mathbf{r}) \tag{2.10}$$

$\boldsymbol{\rho}^e(\mathbf{r})$ and $\boldsymbol{\rho}^h(\mathbf{r})$ are the equivalent electric and magnetic charge densities and are related to the corresponding currents as

$$\nabla \cdot \mathbf{J}(\mathbf{r}) = -j\omega\boldsymbol{\rho}^e(\mathbf{r}) \tag{2.11}$$

$$\nabla \cdot \mathbf{M}(\mathbf{r}) = -j\omega\boldsymbol{\rho}^h(\mathbf{r}) \tag{2.12}$$

The integral equations described above can be discretized using scalar basis functions [23] and can be solved using the method of moments Galerkin formulation [24]. For ease of casting the integral equation in terms of functions that represent physical quantities we will express the equations in slightly different form.

2.3 Solution procedure

2.3.1 Basis functions

The integral equations described above are cast in terms of electric flux density and magnetic flux density which are normally continuous at the media interfaces.

$$\mathbf{J}(\mathbf{r}) = j\omega\kappa_e(\mathbf{r})\mathbf{D}(\mathbf{r}) \tag{2.13}$$

$$\mathbf{M}(\mathbf{r}) = j\omega\kappa_h(\mathbf{r})\mathbf{B}(\mathbf{r}) \tag{2.14}$$

where

$$\kappa_e(\mathbf{r}) = \frac{\epsilon(\mathbf{r}) - \epsilon_o}{\epsilon(\mathbf{r})} \tag{2.15}$$

$$\kappa_h(\mathbf{r}) = \frac{\mu(\mathbf{r}) - \mu_o}{\mu(\mathbf{r})} \tag{2.16}$$

With these new definitions in hand the integral equations can be recast in terms of $\mathbf{D}(\mathbf{r})$ and $\mathbf{B}(\mathbf{r})$. The integral equation can be discretized using scalar basis functions and solved

using the method of moments (MoM). The electric and magnetic flux densities is represented using tetrahedral basis functions proposed by Schaubert *et al.* [23]. These basis functions can be thought of as the three dimensional analogue of rooftop basis functions [25]. The material properties within a tetrahedron are approximated to be constant. The choice of these particular basis functions preserves normal continuity of the flux density. This permits us to represent the spatial variation of the flux density by

$$\mathbf{D}(\mathbf{r}) = \sum_{n=1}^{N} D_n \mathbf{f}_n(\mathbf{r}) \tag{2.17}$$

and

$$\mathbf{B}(\mathbf{r}) = \sum_{n=1}^{N} B_n \mathbf{f}_n(\mathbf{r}) \tag{2.18}$$

N being the number of unknowns and D_n and B_n being the unknown expansion coefficients.

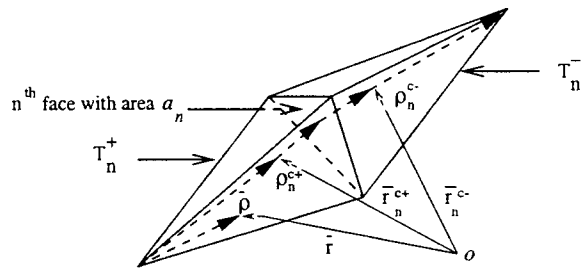

Figure 2.2 Geometrical Parameters associated with the n^{th} face.

The spatial basis function (refer Figure 2.2) associated with the n^{th} face is defined as:

$$\mathbf{f}_n(\mathbf{r}) = \begin{cases} \dfrac{a_n}{3v_n^+}\boldsymbol{\rho}_n^+ & \mathbf{r} \in T_n^+ \\ \dfrac{a_n}{3v_n^-}\boldsymbol{\rho}_n^- & \mathbf{r} \in T_n^- \end{cases} \tag{2.19}$$

where $T_n^{\pm}$ are the pair of tetrahedra that share the n^{th} face, a_n is the area of n^{th} face and $v_n^{\pm}$ is the volume of $T_n^{\pm}$. The vector $\boldsymbol{\rho}_n^+$ is defined from the free vertex of T_n^+ to the position vector $\mathbf{r}$; $\boldsymbol{\rho}_n^-$ is defined similarly except that it is directed towards the free vertex of T_n^-. The subscripts refer to faces and the superscripts refer to tetrahedra. The triangular faces residing on the boundary of V have basis functions that are non zero over a single tetrahedron since only one of it is associated with those faces.

2.3.2 Matrix equations

The integral equation is discretized using a Galerkin testing procedure. Using (2.17) and (2.18) and the symmetric inner product, $< \mathbf{f}_m(\mathbf{r}), \mathbf{g}_n(\mathbf{r}) > = \int_V \mathbf{f}_m(\mathbf{r}) \cdot \mathbf{g}_n(\mathbf{r}) dv$, results in

$$< \mathbf{f}_m(\mathbf{r}), \frac{\mathbf{D}_n(\mathbf{r})}{\epsilon_n(\mathbf{r})} > + j\omega < \mathbf{f}_m(\mathbf{r}), \mathbf{A}_n(\mathbf{r}) > + < \mathbf{f}_m(\mathbf{r}), \nabla\phi_n^e(\mathbf{r}) > + \frac{1}{\epsilon_o} < \mathbf{f}_m(\mathbf{r}), \nabla \times \mathbf{F}_n(\mathbf{r}) > = < \mathbf{f}_m(\mathbf{r}), \mathbf{E}_m^i(\mathbf{r}) > \tag{2.20}$$

$$< \mathbf{f}_m(\mathbf{r}), \frac{\mathbf{B}_n(\mathbf{r})}{\mu_n(\mathbf{r})} > + j\omega < \mathbf{f}_m(\mathbf{r}), \mathbf{F}_n(\mathbf{r}) > + < \mathbf{f}_m(\mathbf{r}), \nabla\phi_n^h(\mathbf{r}) > - \frac{1}{\mu_o} < \mathbf{f}_m(\mathbf{r}), \nabla \times \mathbf{A}_n(\mathbf{r}) > = < \mathbf{f}_m(\mathbf{r}), \mathbf{H}_m^i(\mathbf{r}) > \tag{2.21}$$

Equations (2.20) and (2.21) represent 2N equations for the 2N unknown coefficients D_n and B_n. The submatrix for the m^{th} and n^{th} interaction can be written as

$$\begin{bmatrix} \mathbf{Z}_{ee,mn} & \mathbf{Z}_{eh,mn} \\ \mathbf{Z}_{he,mn} & \mathbf{Z}_{hh,mn} \end{bmatrix} \begin{bmatrix} D_n \\ B_n \end{bmatrix} = \begin{bmatrix} \mathbf{E}_{inc,m} \\ \mathbf{H}_{inc,m} \end{bmatrix} \tag{2.22}$$

where D_n and B_n represent the electric and magnetic current coefficients

$$\mathbf{E}_{inc,m} = \frac{a_m}{3} \left[\frac{1}{v_m^+} \int_{T_m^+} \mathbf{E}_m^i(\mathbf{r}) \cdot \boldsymbol{\rho}_m^{e+} dv + \frac{1}{v_m^-} \int_{T_m^-} \mathbf{E}_m^i(\mathbf{r}) \cdot \boldsymbol{\rho}_m^{e-} dv \right] \tag{2.23}$$

and

$$\mathbf{H}_{inc,m} = \frac{a_m}{3} \left[\frac{1}{v_m^+} \int_{T_m^+} \mathbf{H}_m^i(\mathbf{r}) \cdot \boldsymbol{\rho}_m^{h+} dv + \frac{1}{v_m^-} \int_{T_m^-} \mathbf{H}_m^i(\mathbf{r}) \cdot \boldsymbol{\rho}_m^{h-} dv \right] \tag{2.24}$$

The elements of the interaction matrix are given by

$$\mathbf{Z}_{ee,mn} = < \mathbf{f}_m(\mathbf{r}), \frac{\mathbf{D}_n(\mathbf{r})}{\epsilon_n(\mathbf{r})} > + j\omega < \mathbf{f}_m(\mathbf{r}), \mathbf{A}_n(\mathbf{r}) > + < \mathbf{f}_m(\mathbf{r}), \nabla\phi_n^e(\mathbf{r}) > \tag{2.25}$$

$$\mathbf{Z}_{eh,mn} = \frac{1}{\epsilon_o} < \mathbf{f}_m(\mathbf{r}), \nabla \times \mathbf{F}_n(\mathbf{r}) > \tag{2.26}$$

$$\mathbf{Z}_{hh,mn} = < \mathbf{f}_m(\mathbf{r}), \frac{\mathbf{B}_n(\mathbf{r})}{\mu_n(\mathbf{r})} > + j\omega < \mathbf{f}_m(\mathbf{r}), \mathbf{F}_n(\mathbf{r}) > + < \mathbf{f}_m(\mathbf{r}), \nabla\phi_n^h(\mathbf{r}) > \tag{2.27}$$

$$\mathbf{Z}_{he,mn} = -\frac{1}{\mu_o} < \mathbf{f}_m(\mathbf{r}), \nabla \times \mathbf{A}_n(\mathbf{r}) > \tag{2.28}$$

These integrals are evaluated analytically [23]. The terms $< \mathbf{f}_m, \nabla\phi_n^e >$ and $< \mathbf{f}_m, \nabla\phi_n^h >$ can be expanded as

$$< \mathbf{f}_m(\mathbf{r}), \nabla\phi_n^e(\mathbf{r}) > = \int_S \phi_n^e(\mathbf{r})\mathbf{f}_m(\mathbf{r}) \cdot \hat{\mathbf{n}} ds - \int_V \phi_n^e(\mathbf{r}) \nabla \cdot \mathbf{f}_m(\mathbf{r}) dv \tag{2.29}$$

and

$$< \mathbf{f}_m(\mathbf{r}), \nabla\phi_n^h(\mathbf{r}) > = \int_S \phi_n^h(\mathbf{r})\mathbf{f}_m(\mathbf{r}) \cdot \hat{\mathbf{n}} ds - \int_V \phi_n^h(\mathbf{r}) \nabla \cdot \mathbf{f}_m(\mathbf{r}) dv \tag{2.30}$$

Following a similar procedure the terms $< \mathbf{f}_m(\mathbf{r}), \nabla \times \mathbf{F}_n(\mathbf{r}) >$ and $< \mathbf{f}_m(\mathbf{r}), \nabla \times \mathbf{A}_n(\mathbf{r}) >$ can be expanded as

$$< \mathbf{f}_m(\mathbf{r}), \nabla \times \mathbf{F}_n(\mathbf{r}) > = - \int_S (\mathbf{f}_m(\mathbf{r}) \times \mathbf{F}_n(\mathbf{r})) \cdot \hat{\mathbf{n}} ds \tag{2.31}$$

$$< \mathbf{f}_m(\mathbf{r}), \nabla \times \mathbf{A}_n(\mathbf{r}) > = - \int_S (\mathbf{f}_m(\mathbf{r}) \times \mathbf{A}_n(\mathbf{r})) \cdot \hat{\mathbf{n}} ds \tag{2.32}$$

using the Divergence theorem and under the assumption that

$$\nabla \times \mathbf{f}_m(\mathbf{r}) = 0 \tag{2.33}$$

The volume and the surface integrals are computed using quadrature rules for tetrahedra and triangles respectively [26, 27]. The matrix equation can be solved using a iterative solver like TFQMR for the unknown electric and magnetic flux densities [28].

CHAPTER 3 RESULTS

This section presents results for several test cases that validate the mathematical formulations presented in Chapter 2. To do this we will compare the numerically computed far-field patterns of canonical geometries likes spheres, spherical shells and infinite slabs against analytically obtained scattering spectra.

3.1 RCS of a sphere

The sphere under consideration is immersed in a plane wave with electric field $\mathbf{E}_{inc}$ and magnetic field $\mathbf{H}_{inc}$. The electric field is x polarized and is travelling along the $+z$ direction. The analytical results are obtained using the Mie series expansion [29]. The effective radius obtained from the volume summation of the tetrahedral discretization elements of the sphere. Results are presented for a dielectric sphere of relative permittivity $\epsilon_r = 10$ in Figure 3.1. Excellent agreement is observed between the numerically computed solution and the analytical results. Figure 3.2 illustrates far-field pattern for a magnetic sphere with relative permeability $\mu_r = 10$.

3.2 RCS of a spherical shell

A thin spherical shell is subject to a x polarized plane wave travelling in the $+z$ direction. Figure 3.3 shows a very close agreement between analytical and experimental values of far-field radiation patterns for two instances of a mixed media spherical shell; $\epsilon_r = 4$, $\mu_r = 2$ and $\epsilon_r = 2$, $\mu_r = 2$. As seen, results for both cases match analytical values closely.

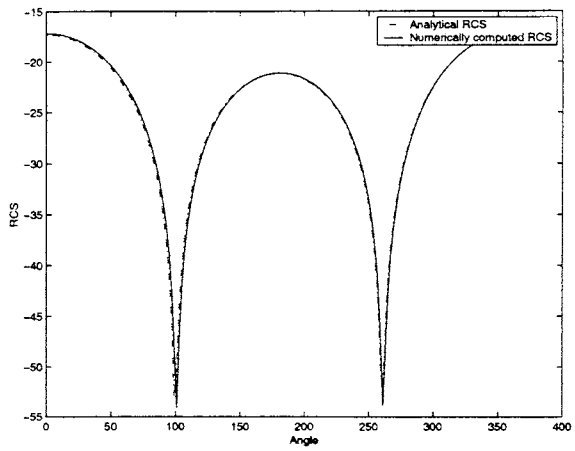

Figure 3.1 RCS pattern of a Dielectric Sphere of $r = 0.01\lambda$, $\epsilon_r = 10$.

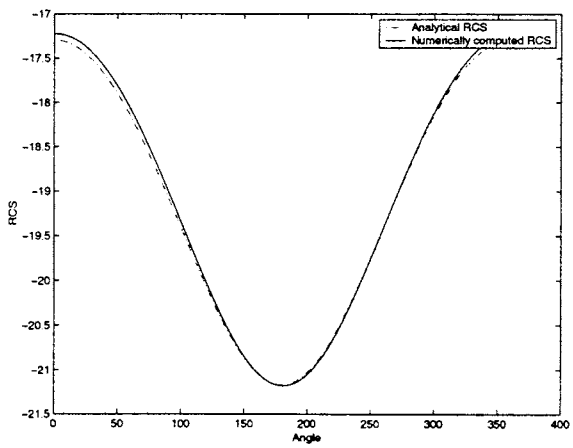

Figure 3.2 RCS pattern of a Magnetic Sphere of $r = 0.01\lambda$, $\mu_r = 10$.

3.3 Validation of periodic Green's function

The periodic Green's function described in the Appendix is validated by calculating the transmission spectra from a slab of finite thickness which is infinite along the other two axes. It is seen that the numerical results agree closely with the analytical results [30].

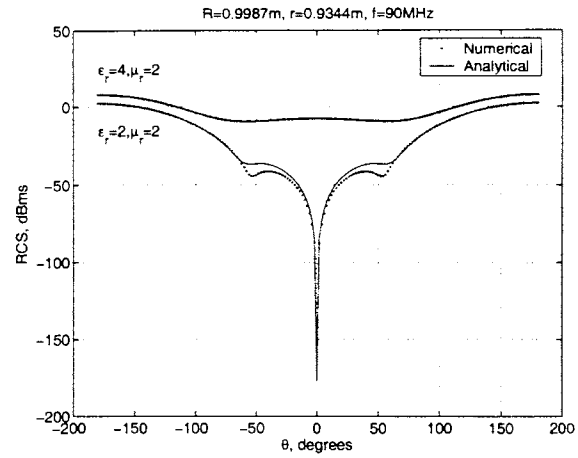

Figure 3.3 Far-field patterns of a thin spherical shell.

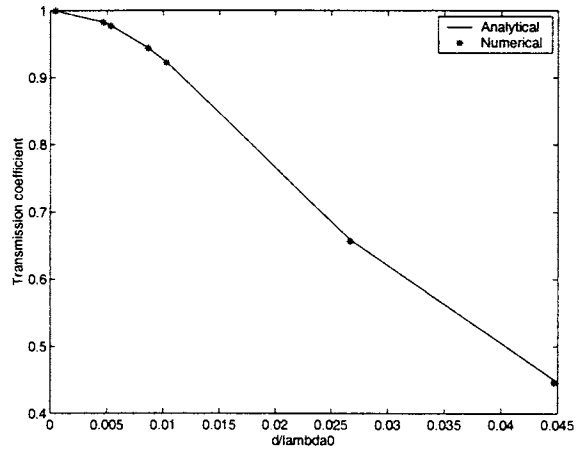

Figure 3.4 Transmission coefficient from a slab of $\epsilon_r = 10$.

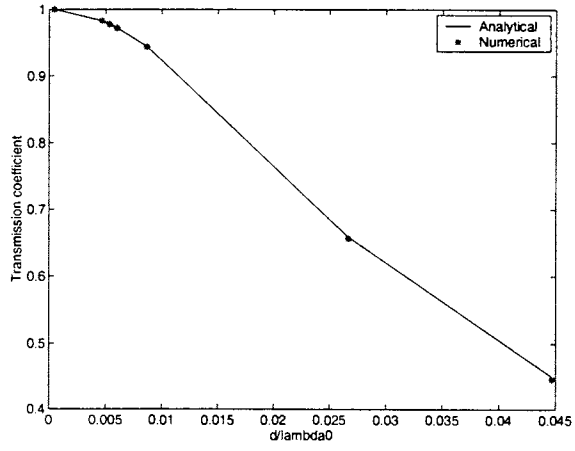

Figure 3.5 Transmission coefficient from a slab of $\mu_r = 10$.

CHAPTER 4 MAGNETICALLY TUNABLE PHOTONIC BAND-GAP STRUCTURES

4.1 Review of band-gap tuning methods

Tunability of band-gap structures in the optoelectronic and microwave ranges opens up a plethora of applications viz. filters, high-Q resonators, lasers etc. Tuning of PBGs has been achieved by infiltrating them with liquid crystals [31, 32, 33] or intrinsic semiconductors [34], floating magnetic particles in a colloidal media [35] or the application of external electric or magnetic field [8, 36].

4.2 Band-gap tuning using external field

Tunable PBGs using ferrites is a very viable option in the microwave ranges since most ferrites have values of μ quite different from 1. Ferrites are operated in the saturated state to minimize losses. The μ depends on the saturation magnetization, the microwave frequency, and the external static magnetic field H_{ex}. It must be noted that in the optical range, the relative permeability of ferrites μ is equal to 1.

Assuming the external static magnetic field in the direction of z. The μ of the ferrite for the transverse magnetic mode subject to such a field remains the same as that of an unbiased ferrite as the dipole moments of the saturated ferrite media do not interact with the external field. However for the transverse electric field, the magnetic field of the mode being perpendicular to H_{ex} effects the μ as shown in Equation (4.1) [37, 38].

$$\mu = \frac{(\omega_{ex} + \omega_m)^2 - \omega^2}{\omega_{ex}(\omega_{ex} + \omega_m) - \omega^2} \tag{4.1}$$

where

$$\omega_{ex} = \mu_o \gamma H_{ex} \tag{4.2}$$

and

$$\omega_m = \mu_o \gamma M_s \tag{4.3}$$

γ is the ratio of the spin magnetic moment to the spin angular momentum, i.e. the gyromagnetic ratio and M_s is the saturation magnetization of the ferrite medium.

4.3 Results

4.3.1 Description of the PBG geometry

The photonic band-gap structure used in the simulations is a two-dimensional structure periodic along two of its axes and homogeneous along the third. It consists of a square lattice of air holes drilled in a material block that 5 layers thick. The radius of the holes is $0.45a$ where a is the lattice spacing [16]. The thickness of each layer is $0.20a$. A diagrammatic representation of this geometry is shown in Figure 4.1.

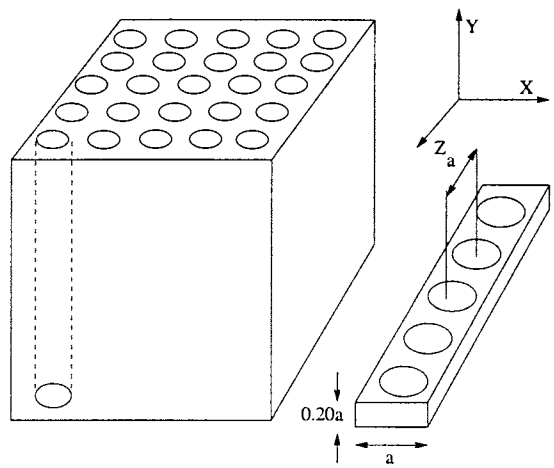

Figure 4.1 5 Layer rectangular PBG.

4.3.2 Dielectric structures

The material slab of the geometry described earlier is assumed to be dielectric with an $\epsilon_r = 10.2$. Reflection spectrum presented in Figure 4.2 displays a TE band-gap corresponding to the normalized frequencies $0.21 \leq a/\lambda_0 \leq 0.28$ for normal plane wave incidence. This agrees well with the results presented in [16].

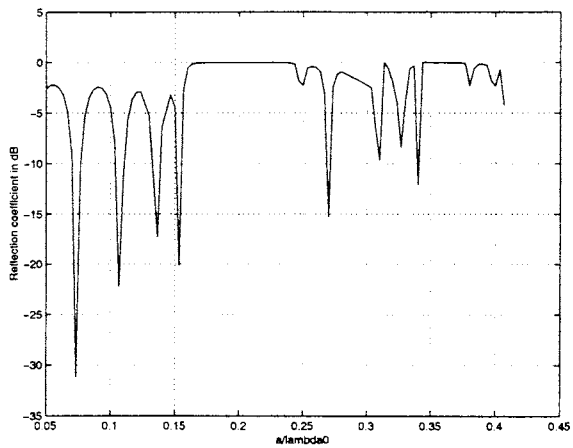

Figure 4.2 Reflection spectrum from Dielectric PBG with $\epsilon_r = 10.2$.

Figures 4.3 and 4.4 display the reflection spectrum for the same geometry with $\epsilon_r = 15.0$ and $\epsilon_r = 20.0$ respectively.

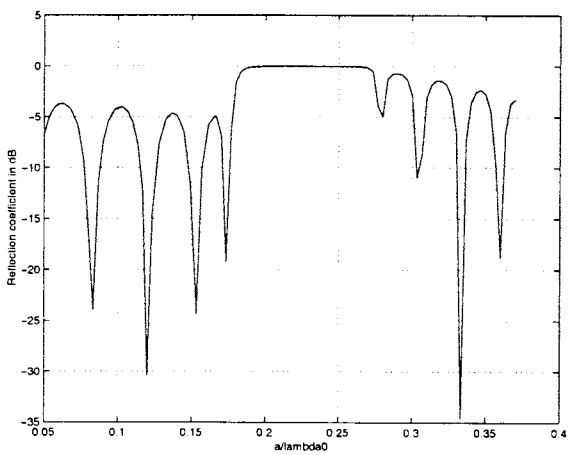

Figure 4.3 Reflection spectrum from Dielectric PBG with $\epsilon_r = 15.0$.

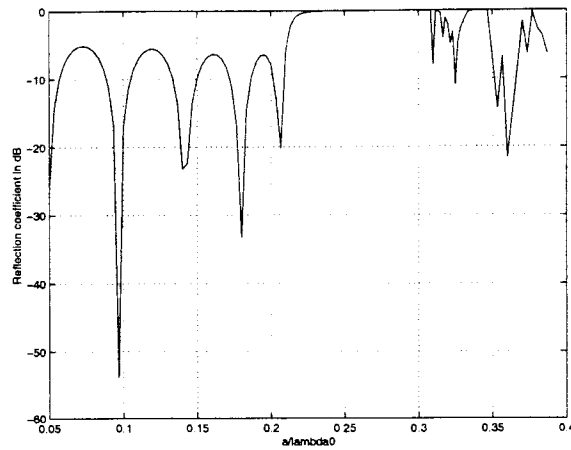

Figure 4.4 Reflection spectrum from Dielectric PBG with $\epsilon_r = 20.0$.

4.3.3 Magnetic structures

Figure 4.5, 4.6 and Figure 4.7 display the reflection and transmission spectrum for a magnetic PBG of $\mu_r = 10.2$, $\mu_r = 15.0$ and $\mu_r = 20.0$ respectively.

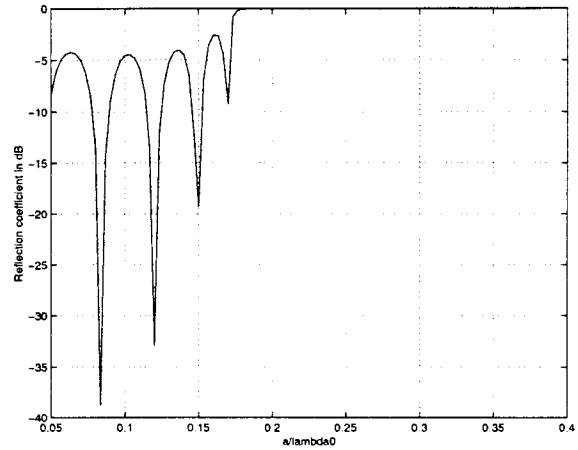

Figure 4.5 Reflection spectrum from Magnetic PBG with $\mu_r = 10.2$.

4.3.4 Dielectric-magnetic structures

Figure 4.8 displays the reflection and transmission spectrum of a dielectric-magnetic PBG of $\epsilon_r = 2.0$ and $\mu_r = 18.0$. From the above figures, it is observed that the center frequency of the band-gap is effected by the changes in the permeability and permittivity of the medium.

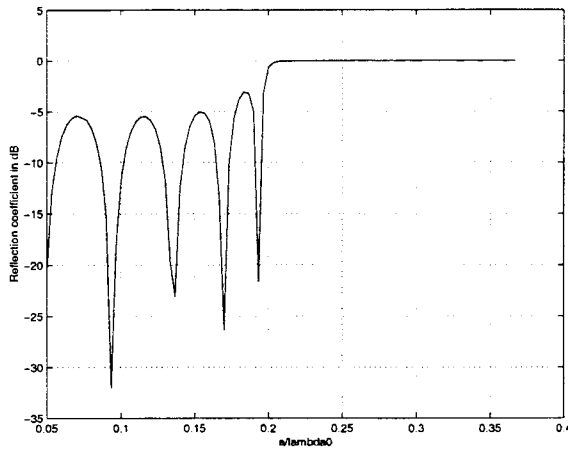

Figure 4.6 Reflection spectrum from Magnetic PBG with $\mu_r = 15.0$.

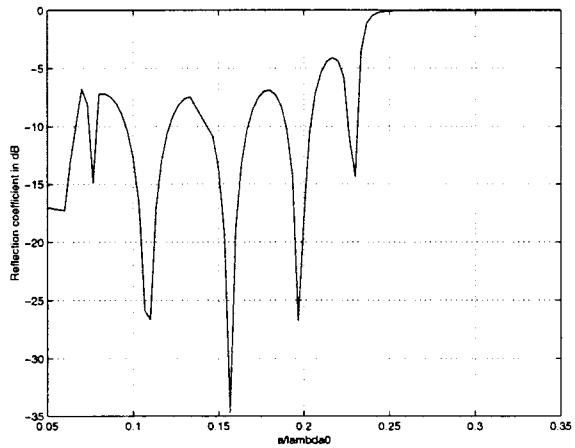

Figure 4.7 Reflection spectrum from Magnetic PBG with $\mu_r = 20.0$.

This validates the fact that a change in the material constant of the medium can be used to tune the band-gap of a photonic structure. Further more, it has been theoretically demonstrated that the magnetic property of the medium can be varied by the application of an external field. In practise, it is more convenient to change the permeability rather than the permittivity.

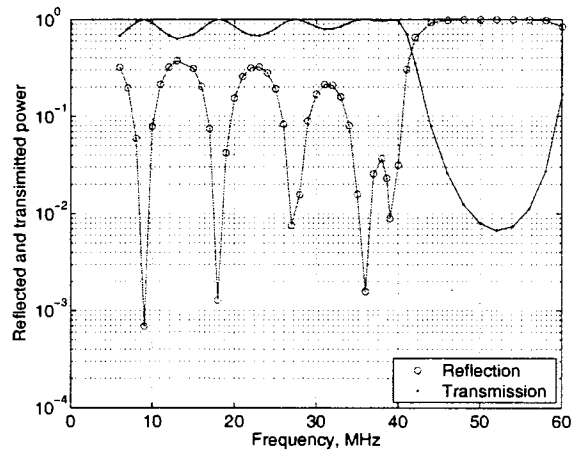

Figure 4.8 Reflection-transmission spectrum from Dielectric-Magnetic PBG with $\epsilon_r = 2.0$ and $\mu_r = 18.0$.

CHAPTER 5 CONCLUSION

This thesis presented an combined field integral equation scheme for inhomogeneous three-dimensional bodies. Periodic Green's function is incorporated into such a scheme and has been validated. This scheme has been applied to photonic band-gap (PBG) structures. It has been demonstrated that by way of numerical simulation that changing the material constant of the PBG structures, the position of the band-gap can be changed. It has been theoretically proved that material constant can be affected by the application of an external static magnetic field. Thus by application of an external field, band-gap tuning can be achieved.

APPENDIX PERIODIC GREEN'S FUNCTION

Integral equation formulations of electromagnetic scattering from periodic structures have as their kernel the free space periodic Green's function. The periodic Green's function may be derived either as a response to an array of line or point sources - the spatial domain or as a response to a series of current sheets i.e. the spectral domain. The spectral and spatial responses form a Fourier transform pair and are slowly convergent summations. The convergence problem in either domain occurs due to the unavoidable singularities in the reciprocal domain. It has been shown that using basis functions with a wide support in the spatial domain speeds up the convergence of summations in the spectral domain [39]. The speed of convergence of the spectral Green's function also depends on whether the point of interest is off-plane or on-plane in the finite dimension of the structure, off-plane points aiding the convergence of the spectral formulation. Several methods have been proposed to overcome this problem,for instance Poisson's transformation, Kummer's transformation, Veysoglu's transformation, Shanks transformations etc [40, 41, 42]. R. E. Jorgenson and R. Mittra have demonstrated by means of numerical experiments that using a combination of both the spectral and spatial domain summations is the most the most accurate and efficient way of computing the periodic Green's function [43]. Details of this method are discussed below.

Consider a planar arrangement of three-dimensional bodies infinitely periodic in the x and y direction. Assume that the unit cell is of dimensions $a \times b$. The incident wave is a plane wave with a direction of propagation θ with respect to the z axis and ϕ with respect to the x axis.

In the spatial domain the currents induced in an unit cell at a point (x,y,z) due to point

sources at (x',y',z') may be represented as

$$\mathbf{J}(x,y,z) = \sum_{m=-\infty}^{\infty}\sum_{n=-\infty}^{\infty} \delta(\boldsymbol{\rho}-\boldsymbol{\rho}'-\boldsymbol{\rho}_{mn})e^{-j\mathbf{k}_o\cdot\boldsymbol{\rho}_{mn}}\delta(z-z') \tag{A.1}$$

where

$$\boldsymbol{\rho}_{mn} = na\hat{\mathbf{x}} + mb\hat{\mathbf{y}} \tag{A.2}$$

The phase shift $\mathbf{k}_o \cdot \boldsymbol{\rho}_{mn}$ is due to the incident wave and can be calculated from Floquet's theorem. The response at each point (x_o,y_o,z_o)may be summed to obtain the spatial-domain periodic Green's function

$$\mathbf{G}_p(\mathbf{r}_o) = \sum_{m=-\infty}^{\infty}\sum_{n=-\infty}^{\infty} e^{-j\mathbf{k}_o\cdot\boldsymbol{\rho}_{mn}} \frac{e^{-jk_o\sqrt{|\boldsymbol{\rho}-\boldsymbol{\rho}'-\boldsymbol{\rho}_{mn}|^2+(z_o-z')^2}}}{4\pi\sqrt{|\boldsymbol{\rho}-\boldsymbol{\rho}'-\boldsymbol{\rho}_{mn}|^2+(z_o-z')^2}} \tag{A.3}$$

Likewise in the spectral domain, the currents can be evaluated as

$$\mathbf{J}(x,y,z) = \frac{1}{ab}\sum_{m=-\infty}^{\infty}\sum_{n=-\infty}^{\infty} e^{j(\mathbf{k}_{mn}-\mathbf{k}_o)\cdot(\boldsymbol{\rho}-\boldsymbol{\rho}')}\delta(z-z') \tag{A.4}$$

ab is the area of the unit cell and the reciprocal translation vector k_{mn} is defined as

$$\mathbf{k}_{mn} = \frac{2\pi n}{a}\hat{\mathbf{x}} + \frac{2\pi m}{b}\hat{\mathbf{y}} \tag{A.5}$$

Adding the response at (x_o,y_o,z_o) of each current sheet, the spectral Green's function can be expressed as

$$\mathbf{G}_p(\mathbf{r}_o) = \frac{1}{ab}\sum_{m=-\infty}^{\infty}\sum_{n=-\infty}^{\infty} \frac{e^{-j\gamma|z_o-z'|}e^{j(\mathbf{k}_{mn}-\mathbf{k}_o)\cdot(\boldsymbol{\rho}-\boldsymbol{\rho}')}}{2j\gamma} \tag{A.6}$$

where application of the radiation condition yields

$$\gamma = \begin{cases} \sqrt{k_o^2-\beta_{xmn}^2-\beta_{ym}^2} & k_o^2 > \beta_{xmn}^2+\beta_{ym}^2 \\ -j\sqrt{\beta_{xmn}^2+\beta_{ym}^2-k_o^2} & \beta_{xmn}^2+\beta_{ym}^2 > k_o \end{cases} \tag{A.7}$$

$$\beta_{xmn} = \frac{2\pi n}{a} - \frac{2\pi m}{b} - k_x \tag{A.8}$$

$$\beta_{ym} = \frac{2\pi m}{h} - k_y \tag{A.9}$$

When $\gamma = 0$, the spectral domain formulation becomes singular and consequently its Fourier pair the spatial domain Green's function converges slowly. On the other hand the spectral formulation converges rapidly when $z_o \neq z'$ i.e. the off-plane case. In order to accelerate the convergence of the spatial domain function (A.3), the asymptotic behavior of $e^{\frac{-jkR}{R}}$ is added to and subtracted from the periodic Green's function by moving off the xy plane cRab units which stands for $c\sqrt{ab}$. The selection of the parameter c determines the weighting given to each domain i.e. how far "off-plane" the point has to be for the spectral formulation to be invoked. Equation (A.3) is modified to

$$\mathbf{G}_p(\mathbf{r}_o) = \mathbf{G}_{p1}(\mathbf{r_o}) + \mathbf{G_{p2}}(\mathbf{r_o}) \tag{A.10}$$

$$\mathbf{G}_{p1}(\mathbf{r}_o) = \sum_{m=-\infty}^{\infty}\sum_{n=-\infty}^{\infty} e^{-j\mathbf{k}_o\cdot\boldsymbol{\rho}_{mn}} \frac{e^{-jk_o\sqrt{|\boldsymbol{\rho}-\boldsymbol{\rho}'-\boldsymbol{\rho}_{mn}|^2+(z_o-z')^2}}}{4\pi\sqrt{|\boldsymbol{\rho}-\boldsymbol{\rho}'-\boldsymbol{\rho}_{mn}|^2+(z_o-z')^2}} \tag{A.11}$$

$$- e^{-j\mathbf{k}_o\cdot\boldsymbol{\rho}_{mn}} \frac{e^{-jk_o\sqrt{|\boldsymbol{\rho}-\boldsymbol{\rho}'-\boldsymbol{\rho}_{mn}|^2+(|z_o-z'|+cRab)^2}}}{4\pi\sqrt{|\boldsymbol{\rho}-\boldsymbol{\rho}'-\boldsymbol{\rho}_{mn}|^2+(|z_o-z'|+cRab)^2}} \tag{A.12}$$

$$\mathbf{G}_{p2}(\mathbf{r}_o) = \sum_{m=-\infty}^{\infty}\sum_{n=-\infty}^{\infty} e^{-j\mathbf{k}_o\cdot\boldsymbol{\rho}_{mn}} \frac{e^{-jk_o\sqrt{|\boldsymbol{\rho}-\boldsymbol{\rho}'-\boldsymbol{\rho}_{mn}|^2+(|z_o-z'|+cRab)^2}}}{4\pi\sqrt{|\boldsymbol{\rho}-\boldsymbol{\rho}'-\boldsymbol{\rho}_{mn}|^2+(|z_o-z'|+cRab)^2}} \tag{A.13}$$

Equation (A.11) remains in the spatial domain and converges rapidly because the asymptotic behavior is subtracted out. Equation (A.13) is smooth, non-singular and slowly converging. Its convergence is accelerated by means of Poisson's summations formula.

The above approximation is highly efficient and accurate. An appropriate selection of the parameter c will distribute the computation evenly among the spectral and spatial domains.

Bibliography

[1] J. D. Joannopoulos, R. D. Meade and J. N. Winn. *Photonic crystals: molding the flow of light* . Princeton University Press, Princeton, N. J., 1995.

[2] E. Yablonovitch. Photonic Band Structure: The Face-centered-cubic Case. *Phys. Rev. Lett.*, 63: 1950-3, 1989.

[3] H. S. Sozuer and J. W. Haus. Photonic Bands: Simple-cubic Lattice. *J. Opt. Soc. Am. B*, 10: 296-302, 1993.

[4] P. R. Villeneuve and M. Piche. Photonic Band Gaps in Two-dimensional Square Lattices: Square and Circular Rods. *Phys. Rev. B*, 46: 4973-5, 1992.

[5] A. A. Maradudin and A. R. McGurn. Photonic Band Gaps in Two-dimensional Square and Hexagonal Lattices. *Phys. Rev. B*, 46: 4969-71, 1992.

[6] P. L. Gourley, J. R. Wendt, G. A. Vawter, T. M. Brennan, and B. E. Hammons. Optical Properties of Two-dimensional Photonic Lattices Fabricated as Honey-comb Nanostructures in Compound Semiconductors. *Appl. Phys. Lett.*, 64: 687-9, 1994.

[7] J. M. Gerard, A. Izrael, J. Y. Marzin, R. Padjen, and F. R. Ladan. Photonic Bandgap of Two-dimensional Dielectric Crystals. *Solid-state Electronics*, 37: 1341-4, 1994.

[8] C.-S. Kee, J.-E. Kim, H. Y. Park, I. Park and H. Lim. Two-dimensional tunable magnetic photonic crystals. *Phys. Rev. B*, 61(3): 15523-25, 2001.

[9] G. Parker and M. Charlton. Photonic Crystals. *Physics World*, August 2000.

[10] E Yablanovitch. Inhibited spontaneous emission in solid-state physics and electronics. *Physics Rev. Lett*, 58: 2059.

[11] S. John. Strong Localization of Photons in Certain Disordered Dielectric Superlattices. *Phys. Rev. Lett.*, 58: 2486, 1987.

[12] J. G. Fleming and S. Y. Lin. Three-dimensional photonic crystal with a stop band from 1.35 to 1.95. *Opt. Lett.*, 24(1): 49-51, 1999.

[13] K. M. Ho, C. T. Chan and C. M. Soukoulis. Existence of Photonic Gap in Periodic Dielectric Structures. *Phys. Rev. Lett.*, 65(25): 3152-55, 1990.

[14] H. S. Sozuer, J. W. Haus and R. Ingua. Photonic bands: Convergence problems with plane wave method. *Phys. Rev. B*, 45: 296-302, 1992.

[15] H. Y. Yang. Photonic Band Structures for a Class of 2D Periodic Dielectric Materials. *IEEE MTT-S Digest*, 1996.

[16] Y. Rahmat-Samii and H. Mosallaei. Electromagnetic Band-Gap Structures: Classification, Characterization, and Applications. *11th International Conference on Antennas and Propagation* 560, 2001.

[17] J. C. Chen, H. A. Haus, J. N. Winn, S. Fan and J. D. Joannopoulos. *Guided Wave Optoelectronics: Device Characterization, Analysis and Design.* Plenum Press, New York, 1995.

[18] J. M. Generowicz, B. P. Hiett, S. J. Cox, M. Molinari, D. Beckett and K. S. Thomas. Finite Element Modelling of Photonic Crystals. *3rd Conference on Postgraduate Research in Electronics, Photonics, Communications and Software PREP 2001.*

[19] J. B. Pendry and A. MacKinnon. Calculation of photon dispersion relation. *Phys. Rev. Lett.*, 69: 2772-5, 1992.

[20] M. Scalora and M. E. Crenshaw. A beam propagation method that handles reflections. *Optics Commun.*, 108: 191-6, 1994.

[21] K. M. Leung. Defect modes in photonic band structures: A Green's function approach using vector Wannier functions. *J. Opt. Soc. Am. B*, 10: 303-6, 1993.

[22] C.-S. Kee, Y.-K. Ha, J.-E. Kim, H. Y. Park and H. Lim. Role of Wave Impedance and Refractive Index in Photonic Crystals with Magnetic and Dielectric Properties. *IEEE Trans. on Microwave Theory and Techniques* , 47(11): 2148-50, 1999.

[23] D. H. Schaubert, D. R. Wilton, and A. W. Glisson. A tetrahedral modeling method for electromagnetic scattering by arbitrarily shaped inhomogeneous dielectric bodies. *IEEE Trans. on Antennas and Propagation*, 32(1): 77-85, January 1984.

[24] R. F. Harrington. *Electromagnetic Wave Propagation, Radiation, and Scattering.* Prentice Hall, New York, 1991.

[25] S. M. Rao, D. R. Wilton, and A. W. Glisson. Electromagnetic scattering by surfaces of arbitrary shape. *IEEE Trans. on Antennas and Propagation*, 30(3): 409-18, May 1982.

[26] K. S. Sunder and R. A. Cookson. Integration points for triangles and tetrahedrons abtained from the gaussian quadrature points for a line. *Computers and Structures*, 21(5): 881-5, 1985.

[27] P. Keast. Moderate-degree tetrahedral quadrature formulas. *Computer Meth. Appl. Mechanics Eng.*, 55:339–348, 1986.

[28] Y. Saad. *Iterative methods for sparse linear systems.* PWS series in computer science. PWS Pub. Co., Boston, 1996.

[29] A. Ishimaru. *Field Computation by Moment Methods.* Macmillan, New York, 1968.

[30] N. Ida. *Microwave NDT.* Kluwer Academic Publishers, Netherlands, 1992.

[31] Kurt Busch and Sajeev John. Liquid-Crystal Photonic-Band-Gap Materials: The Tunable Electromagnetic Vacuum. *Phys. Rev. Lett.*, 83(5): 967-970, 1999.

[32] K. Yoshino, Y. Shimoda, Y. Kawagishi, K. Nakayama, and M. Ozaki. Temperature tuning of the stop band in transmission spectra of liquid-crystal infiltrated synthetic opal as tunable photonic crystal. *Appl. Phys. Lett.*, 75: 932, 1999.

[33] C.-S. Kee, H. Lim, Y.-K. Ha, J.-E. Kim, and H. Y. Park. Two-dimensional tunable metallic photonic crystals infiltrated with liquid crystals . *Phys. Rev. B*, 64(8): 085114, 2001.

[34] P. Halevi and F. Ramos-Mendieta . Tunable Photonic Crystals with Semiconducting Constituents . *Phys. Rev. Lett.*, 85: 1875, 2000 .

[35] M. Golosovsky, Y. Saado, and D. Davidov . Self-assembly of floating magnetic particles into ordered structures : A promising route for the fabrication of tunable photonic band gap materials . *Appl. Phys. Lett.*, 75(26): 4168-70, 1999.

[36] A. Figotin and Y. A. Godin. Two-dimensional tunable photonic crystals. *Phys. Rev. B* , 57(5): 2841-48, 1998.

[37] D. M. Pozar. *Microwave Engineering, 2nd ed.*. John Wiley and Sons, Inc., New York, 1998.

[38] M. S. Sodha and N. C. Srivastava. *Microwave Propagation in Ferrimagnetics.* Plenum Press, New York, 1981.

[39] C. H. Tsao and D. R. Wilton. Spectral-domain analysis of frequency selective surfaces comprised of periodic arrays of cross dipoles and Jerusalem crosses. *IEEE Trans. on Antennas and Propagation*, 32: 478-86, May 1984.

[40] S. Singh, W. F. Richards, J. R. Zinecker and D. R. Wilton. Accelerating the convergence of Series Representing the Free Space Periodic Green's Function. *IEEE Trans. on Antennas and Propagation*, 38: 1958-62, December 1990.

[41] A. W. Mathis and A. F. Peterson. A comparison of acceleration procedures for the two-dimensional periodic Green's function. *IEEE Trans. on Antennas and Propagation*, 44: 567-71, April 1996.

[42] A. F. Peterson, S. L. Ray and R. Mittra. *Computational Methods for Electromagnetics.* IEEE, Inc., New York, 1998.

[43] R. E. Jorgenson and R. Mittra. Efficient calculation of the Free-Space Periodic Green's Function. *IEEE Trans. on Antennas and Propagation*, 38: 633-42, May 1990.

ACKNOWLEDGEMENTS

I would like to take this opportunity to express my thanks to those who helped me with various aspects of conducting research and the writing of this thesis. First and foremost, Dr. Shanker Balasubramaniam for his guidance and support throughout this research and the writing of this thesis. I would also like to thank my committee members for their efforts and contributions to this work: Dr. Mani Mina and Dr. Paul Sacks. Special thanks to Dr. Rana Biswas (Ames Laboratory) for his helpful insights. I owe much to the present and past members of the Computational Electromagnetics Group: Dr.Gregory Kobidze, Sridharan Balasubramaniam, Subramanian Lalgudi and Gao Jun for the helpful discussions I had with them. Thanks also to Dr. James Coyle, High Performance Computing Group for computational support. I bear special regard for my friends - Sashisekaran Thiagarajan, Sunitha Kambhampati and Samyukta Sankaran, whose cheerful company has greatly offset the rigors of graduate study.